

PAPER • OPEN ACCESS

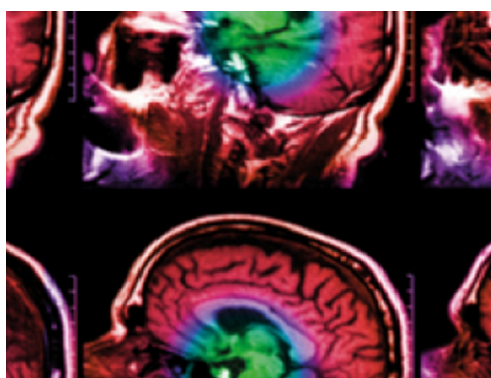
Retrieval of the conductivity spectrum of tissues *in vitro* with novel multimodal tomography

To cite this article: M Lehti-Polojärvi *et al* 2021 *Phys. Med. Biol.* **66** 205016

View the [article online](#) for updates and enhancements.

You may also like

- [Density estimation of grey-level co-occurrence matrices for image texture analysis](#)
Anders Garpebring, Patrik Brynolfsson, Peter Kuess *et al.*
- [Motion correction for PET data using subspace-based real-time MR imaging in simultaneous PET/MR](#)
Thibault Marin, Yanis Djebra, Paul K Han *et al.*
- [Time-resolved versus time-integrated portal dosimetry: the role of an object's position with respect to the isocenter in volumetric modulated arc therapy](#)
Lotte E J R Schyns, Lucas C G G Persoon, Mark Podesta *et al.*



IPEM | IOP

Series in Physics and Engineering in Medicine and Biology

Your publishing choice in medical physics,
biomedical engineering and related subjects.

Start exploring the collection—download the
first chapter of every title for free.



PAPER

OPEN ACCESS








RECEIVED
11 May 2021REVISED
22 September 2021ACCEPTED FOR PUBLICATION
29 September 2021PUBLISHED
14 October 2021

Original content from this work may be used under the terms of the [Creative Commons Attribution 4.0 licence](#).

Any further distribution of this work must maintain attribution to the author(s) and the title of the work, journal citation and DOI.



Retrieval of the conductivity spectrum of tissues *in vitro* with novel multimodal tomography

M Lehti-Polojärvi^{1,3,*} , M J Räsänen^{2,3} , L E Viiri¹ , H Vuorenpää¹ , S Miettinen¹ , A Seppänen²  and J Hyttinen¹ 

¹ Faculty of Medicine and Health Technology, Tampere University, Tampere, Finland

² Department of Applied Physics, University of Eastern Finland, Kuopio, Finland

³ Authors contributed equally.

* Author to whom any correspondence should be addressed.

E-mail: mari.lehti-polojarvi@tuni.fi and mikko.rasanen@uef.fi

Keywords: electrical impedance tomography (EIT), hybrid imaging, limited angle tomography, optical projection tomography (OPT), rotational multifrequency electrical impedance tomography (R-mfEIT), tissue engineering

Supplementary material for this article is available [online](#)

Abstract

Objective: Imaging of tissue engineered three-dimensional (3D) specimens is challenging due to their thickness. We propose a novel multimodal imaging technique to obtain multi-physical 3D images and the electrical conductivity spectrum of tissue engineered specimens *in vitro*. **Approach:** We combine simultaneous recording of rotational multifrequency electrical impedance tomography (R-mfEIT) with optical projection tomography (OPT). Structural details of the specimen provided by OPT are used here as geometrical priors for R-mfEIT. **Main results:** This data fusion enables accurate retrieval of the conductivity spectrum of the specimen. We demonstrate experimentally the feasibility of the proposed technique using a potato phantom, adipose and liver tissues, and stem cells in biomaterial spheroids. The results indicate that the proposed technique can distinguish between viable and dead tissues and detect the presence of stem cells. **Significance:** This technique is expected to become a valuable tool for monitoring tissue engineered specimens' growth and viability *in vitro*.

1. Introduction

Multifrequency electrical impedance tomography (mfEIT) is an imaging technique that reconstructs electrical conductivity images based on surface current excitations and voltage measurements acquired at several frequencies. This imaging technique could find significant applications in the field of tissue engineering, where three-dimensional (3D) biomaterial constructs are combined with stem cell-derived cells. These constructs show great potential in *in vitro* disease models, toxicology studies, drug development, and precision medicine (Fang and Eglen 2017, Gomes *et al* 2017). The imaging of mesoscopic scale (1 mm to 10 mm) 3D specimens is challenging using conventional optical microscopy techniques due to limited penetration depth. Additionally, many of these techniques require staining or clearing the specimens, which eventually kills the cells and renders the biological specimens unusable for further study. For example, an x-ray microtomography method to image the subcellular structures of 3D specimens has been proposed, but the method is only available for fixed specimens (Tamminen *et al* 2020). In order to create novel technologies for non-harmful live 3D imaging, we propose a multimodal tool in which mfEIT is integrated with optical projection tomography (OPT).

In OPT (Sharpe *et al* 2002), multiple projection images are acquired from a rotating specimen to enable full 3D image reconstruction. OPT has been applied to, for example, the characterization of hydrogels (Figueiras *et al* 2014) and the imaging of cells in 3D hydrogels (Belay *et al* 2021). OPT operates in either brightfield or fluorescence mode. Since fluorescence imaging requires autofluorescent or stained specimens, we focus on applying brightfield, i.e. transmission OPT.

Electrical impedance measurements, either spectroscopic or tomographic, do not require staining to obtain information on, for example, cell membrane integrity (Klößgen *et al* 2011), cell–cell contact maturation (Savolainen *et al* 2011), or cell aggregate localization (Wu *et al* 2018). EIT, or in case several frequencies are applied, mFEIT, images the electrical conductivity distribution (absolute mode) or its temporal changes (difference mode). EIT is a non-harmful and fast 3D imaging technique that has been used for the viability detection of cell cultures (Wu *et al* 2018).

The limitation of EIT is typically poor spatial resolution due to its diffusive nature and the associated mathematical ill-posedness of the image reconstruction problem. To tackle this, multimodal imaging techniques have been proposed, where *a priori* information provided by another imaging modality is incorporated into the EIT image reconstruction (Kaipio *et al* 1999). In medical imaging, ultrasound images have been successfully used as a structural prior, for example in Borsic *et al* (2010), Soleimani (2006). A dual-modal sensor that combines EIT and optical microscopy has been presented for *in vitro* applications (Liu *et al* 2020).

We aim to provide multi-physical images and enhanced mFEIT image quality via prior information provided by OPT. We are unaware of previous studies that would have attempted to combine microscopy-scale, optical-based 3D imaging, such as OPT, with mFEIT to perform *in vitro* specimen conductivity analysis. In our system, mFEIT and OPT data are collected simultaneously. The electrode array used for mFEIT covers only a limited portion of the imaging chamber's surface to allow access for OPT acquisition. The problem associated with having only limited angle access to the boundary—both in OPT and mFEIT—is resolved by rotating the specimen step-wise and carrying out the measurements sequentially at multiple rotational positions.

The feasibility of the rotational EIT setup with limited electrode coverage has previously been demonstrated in a two-dimensional (2D) circular setup (Lehti-Polojärvi *et al* 2018) and a 2D rectangular setup (Lehti-Polojärvi *et al* 2019, Winkler *et al* 2020, Lehti-Polojärvi *et al* 2021) using phantoms. In these studies, however, the structural information provided by OPT had not been fused into the mFEIT reconstruction. Further, mFEIT was based on 2D modeling and linearized difference imaging and yielded only qualitative reconstructions of the conductivity. Nevertheless, these studies have demonstrated that the rotational limited angle data acquisition scheme enables the EIT/mFEIT reconstruction while also providing space for OPT. In addition to multimodality, the benefits of this EIT scheme are that it enables a large number of independent measurements and reduces the complexity of the electronics, as a relatively small number of electrodes are needed.

In this study, we extend the rotational mFEIT (R-mFEIT) impedance measurement setup and image reconstruction methods to 3D and, above all, combine data from two imaging modalities by utilizing the structural information from OPT to enhance the conductivity reconstruction in R-mFEIT. This data fusion is achieved by extracting 3D segmentation from OPT reconstructions and incorporating this information into 3D R-mFEIT image reconstruction using rotational meshing and Bayesian inversion methods, finally yielding estimates for the electrical conductivity spectra of the segments.

We test the feasibility of the proposed multimodal technique experimentally. First, the imaging technique is evaluated with a potato inclusion with a controlled shape and known frequency response. Next, the ability of OPT-mFEIT to differentiate the conditions of tissues (especially their viability) is tested by imaging specimens of adipose and liver tissues before and after chemical or thermal treatment. Finally, we carry out a preliminary experiment on human induced pluripotent stem cells (iPSCs) in biomaterial spheroids—an application that will in future be the main target of the developed multimodal imaging system.

2. Methods and materials

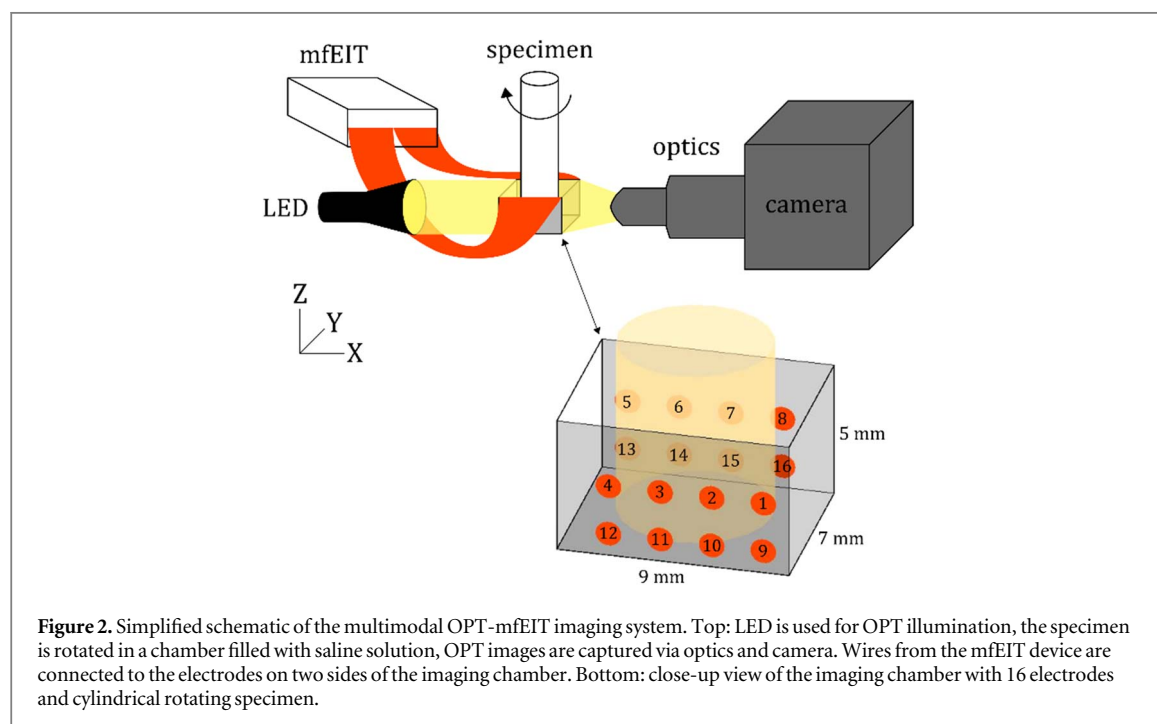
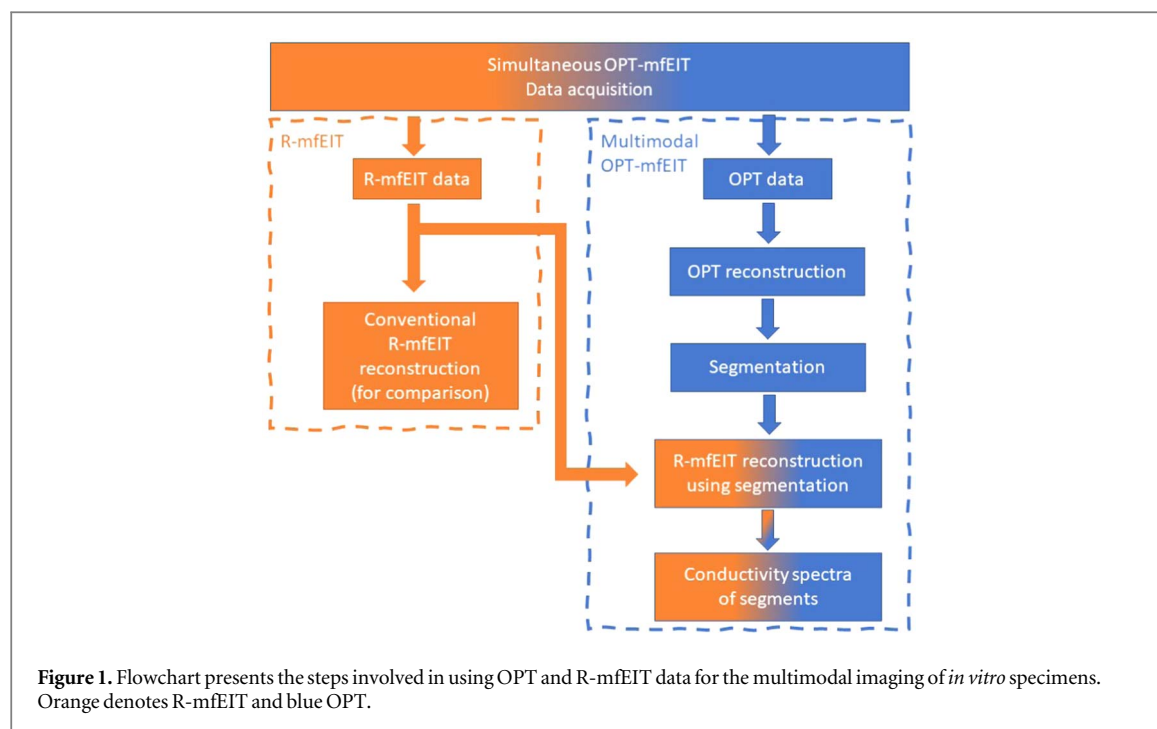
2.1. Overview of the multimodal imaging

Figure 1 summarizes the steps used in multimodal OPT-mFEIT imaging. The raw R-mFEIT data consist of electrical impedance values and OPT data consist of 2D projection images acquired from several rotational positions. The R-mFEIT data was used both for conventional R-mFEIT reconstruction and for multimodal OPT-mFEIT reconstruction. The conventional R-mFEIT reconstruction served as a comparison to the integrated OPT-mFEIT reconstruction approach, and as a check of the quality of the measured R-mFEIT data.

OPT data were used for reconstructing the light absorption distribution within the imaging domain. The 3D OPT reconstruction was segmented to extract the morphology and location of the specimen. The segmentation was then integrated into the R-mFEIT reconstruction process in order to directly estimate the conductivity spectra of the segmented regions from the R-mFEIT data.

2.2. Multimodal system design

Our R-mFEIT technique was designed to be combined with an in-house-built OPT system (Figueiras *et al* 2014, Belay *et al* 2021). A schematic of the OPT-mFEIT system is shown in figure 2.



The main parts of OPT are illumination, specimen rotation stage, and light detection. We used a white LED (irradiance maximum 2.8 mW cm^{-2}) for brightfield parallel beam illumination. The specimens were attached from the top to a motorized stage (Standa Ltd, Lithuania) with rotational and x - y - z movements for proper specimen alignment. The imaging chamber had two transparent glass walls for OPT, and it was filled with saline solution. Saline was used to enable both a refractive index matching path for illumination and suitable electrical conductivity between the electrodes and the specimen. The optical detection system consisted mainly of a $2\times$ objective lens (Edmund Optics, USA), an iris diaphragm (Thorlabs, USA), a tube lens (Mitutoyo, USA), and an sCMOS camera (ORCA-Flash 4.0, Hamamatsu, Japan).

Fluorinated ethylene propylene (FEP) tubes (5 mm inner diameter, 6 mm outer diameter, Adtech Polymer Engineering Ltd, UK) were used to attach the hydrogel-based specimen to the rotational stage. To allow electrical contact, approximately 3 mm of the hydrogel with the embedded inclusion(s) was pushed out of the insulating tube during imaging.

An mFEIT device that generates binary multifrequency excitation (Min *et al* 2018) was used for impedance measurements. The current excitations were carried out using 15 frequencies ranging from 1 to 349 kHz, which is typically in the β -dispersion region of biological samples (Klößgen *et al* 2011). The device had a multiplexer with 16 bi-directional input/output channels for tetrapolar impedance measurements.

MFEIT electrodes were fabricated on two flexible Kapton-based sheets and attached to two opposing walls of the rectangular imaging chamber. These 16 electrodes (1 μ m copper coated with 50 nm gold layer), shown in figure 2, were connected to the mFEIT device via zero insertion force connectors (Würth Elektronik, Germany) and wires that were as short as possible to reduce noise.

2.3. Rotational data acquisition

Simultaneous OPT-mFEIT data acquisitions were performed with a custom-made LabVIEW program (Yuan 2020). OPT images were acquired every 0.9° over 360° rotation, and the R-mFEIT measurements were saved at 4.5° intervals.

The measurement pattern applied at every R-mFEIT rotational position was designed for our limited angle electrode layout (see figure 2). The pattern contained 30 pairwise current excitation configurations and 13 pairwise voltage measurements for each excitation, providing 390 tetrapolar measurements. The first 15 excitations were applied sequentially between electrode 2 and each of the other 15 electrodes. Correspondingly, in the second set of excitations, currents were injected between electrode 14 and the other 15 electrodes. Voltage measurements were obtained sequentially between the electrode adjacent to the current excitation electrode and the rest of the electrodes. Current excitation electrodes were not included in the voltage sensing. The measurement pattern is visualized in supplementary materials (available online at stacks.iop.org/PMB/66/205016/mmedia). The design of the current excitation and voltage measurement configurations was based on the lead field theory (Geselowitz 1971) to obtain measurement patterns with high sensitivity in the entire volume of the specimen.

Total data acquisition time depended on several factors, such as camera exposure time, the number of measurement angles, and the number of repeated impedance measurements for averaging. We used an exposure time of approximately 1.2 ms, and the number of projection images taken for OPT was 400. For R-mFEIT, measurements were collected from 80 rotational positions, resulting in $80 \times 390 = 31\,200$ measurements. Each tetrapolar measurement was taken as the average of seven repeated measurements, resulting in a measuring time of 10 ms for each measurement. With these settings, the total imaging time was approximately 15 min. We note, however, that the amount of data acquired here was excessive and was only measured to ensure that no relevant information was lost in the experiment. Only the R-mFEIT data corresponding to the latter half of the full rotation were used in the image reconstruction.

For each R-mFEIT data acquisition, a reference measurement with only saline present in the imaging chamber was taken. The OPT projections and measured R-mFEIT data are visualized for each specimen type in supplementary materials. The real part of the measured impedance values Z was converted to voltages U with 1 mA current I , as $U = \text{Re}(Z)I$. The videos show the difference between the angular data and the initial position data to clarify the changes due to rotation.

2.4. Estimation of noise statistics

An estimate for the level of the overall noise introduced by the electrodes, wiring, and the mFEIT device was obtained from 1000 repeated blank saline solution measurements in the imaging chamber. The signal-to-noise ratio (SNR) of the R-mFEIT imaging system was calculated as follows:

$$\text{SNR} = 10 \log \frac{\sum_{n=1}^N [y(n)]^2}{\sum_{n=1}^N [y(n) - \bar{y}]^2}, \quad (1)$$

where $N = 1000$ is the number of repeated measurements, $y(n)$ the n th measured voltage value, and \bar{y} the average of N repeated voltage data. The SNR value depends on the measurement configuration, that is, the relative positions of the excitation and measurement electrodes and the applied frequency. For a low sensitivity configuration, the minimum SNR was (5 ± 2) dB, and for a high sensitivity configuration, the maximum SNR was (55 ± 3) dB. According to the applied frequency, the minimum SNR was (32 ± 9) dB at 1 kHz and the maximum was (40 ± 9) dB at 251 kHz.

The reciprocity error is another commonly used metric to evaluate the accuracy of EIT systems. It was calculated from two tetrapolar measurements that applied the same electrodes but interchanged current excitation and voltage measurement pairs. The repeated measurements' percentage error was between 0.1% and 0.7%, depending on the applied frequency.

The covariance of the measurement noise was also estimated for each frequency based on the same repeated measurements. The sample covariance for measurements at given frequency f was the following:

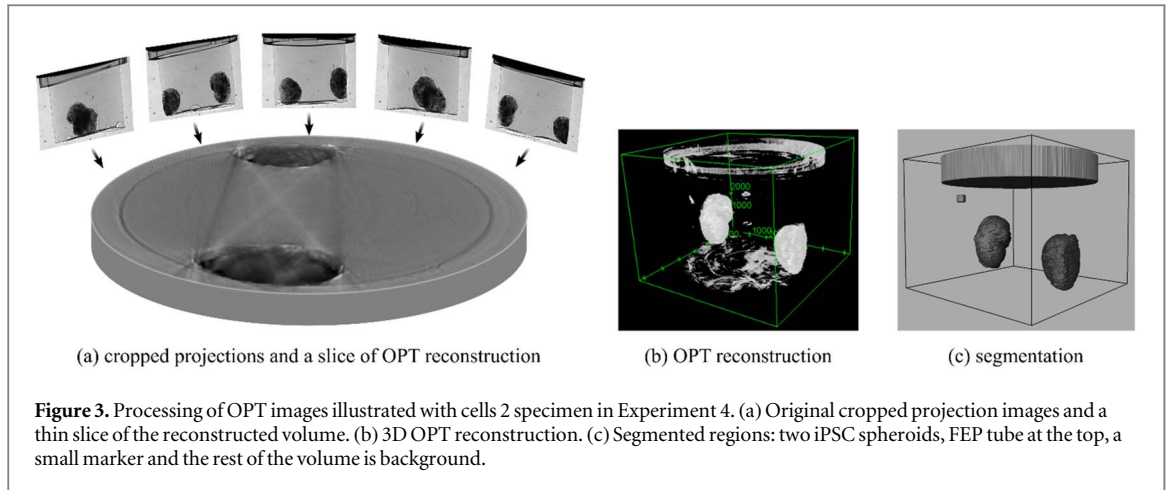


Figure 3. Processing of OPT images illustrated with cells 2 specimen in Experiment 4. (a) Original cropped projection images and a thin slice of the reconstructed volume. (b) 3D OPT reconstruction. (c) Segmented regions: two iPSC spheroids, FEP tube at the top, a small marker and the rest of the volume is background.

$$\Gamma_e^f = \frac{1}{N-1} \sum_{i=1}^N (V_i^f - V_*^f)(V_i^f - V_*^f)^T, \quad (2)$$

where the superscript f refers to the frequency, vector V_i^f is the i th realization of the complete set of voltage measurements corresponding to all injected currents at frequency f , and vector V_*^f is the mean of the repeated voltage measurements. The noise covariance matrix was used when computing the R-mfEIT reconstructions.

2.5. OPT image reconstruction and segmentation

Before computing OPT reconstructions, the R-mfEIT chamber walls were cropped from the sides and bottom of the projection images to save memory. Possible offsets in the specimen's center-of-rotation were manually corrected. This was achieved by reconstructing the top and bottom slices of the specimen with different offset values and visually choosing the best values for each specimen, as in Koskela *et al* (2021). The center-of-rotation was corrected for the rest of the volume by interpolating the top and bottom offsets, as is explained in Figueiras *et al* (2014). OPT reconstructions were computed using a filtered back-projection algorithm (Natterer 2001) implemented in the built-in function `iradon` of MATLAB R2019a (The MathWorks, Inc.). The principle of back-projection from projection images is visualized in figure 3(a). The applicable codes are available at [\[https://github.com/llkskl/fbp-cor\]](https://github.com/llkskl/fbp-cor). OPT reconstructions were visualized with the open-source software Fiji.

The grayscale 3D OPT reconstructions, as the one shown in figure 3(b), were segmented into four regions shown in figure 3(c): inclusion(s), background, FEP tube, and a manually applied marker. The inclusions were the main regions of interest, namely, pieces of tissue or iPSC spheroids. The background was composed of the cylindrical hydrogel scaffold and saline solution. The tube, from which the hydrogel was emerging, is seen as an annular-shaped piece on top of the 3D images in figures 3, 4 and 6. A small cut was made in the tube before specimen preparation to verify the correct orientation of the segmentation during R-mfEIT mesh creation. The marker was added below this cut in the segmentation. After the mesh creation, the marker was removed from further computations.

Segmentations were performed and visualized in Avizo (Thermo Scientific, v.2019.4). First, the OPT reconstructions were resampled from the original $3.25 \mu\text{m}$ voxel size to $13 \mu\text{m}$ voxel size to lighten the image processing. Then, the image stacks were 3D median filtered with a neighborhood of six voxels to slightly smooth the image volume while preserving the edge information. Many of the image stacks were slightly challenging to segment, as some of the inclusion(s) grayscale values were close to the background values. Thus, we mainly used manual thresholding (Magic Wand tool) for the inclusion segments and made corrections with morphological operations and the Lasso tool. The tube and the marker were segmented by generating two ellipses and interpolating a cylinder between them. The rest of the volume was labeled as background. Finally, the segments were 3D smoothed and exported to Matlab to include them in the R-mfEIT finite element (FE) model.

2.6. R-mfEIT modeling and image reconstruction

This section discusses the mathematical models and computational methods used in the R-mfEIT and OPT-mfEIT image reconstruction. We start by briefly reviewing the complete electrode model (CEM), which mathematically describes the dependence of the electrode potentials on the injected currents and electrical conductivity within the volume. This model (or its numerical approximation) is referred to as the forward model of EIT. Next, we review an image reconstruction method that combines the R-mfEIT measurements, CEM, and a smoothness promoting prior model for the electrical conductivity. This method, which does not utilize the structural information given by OPT, is referred to as the conventional reconstruction method. In this study, the

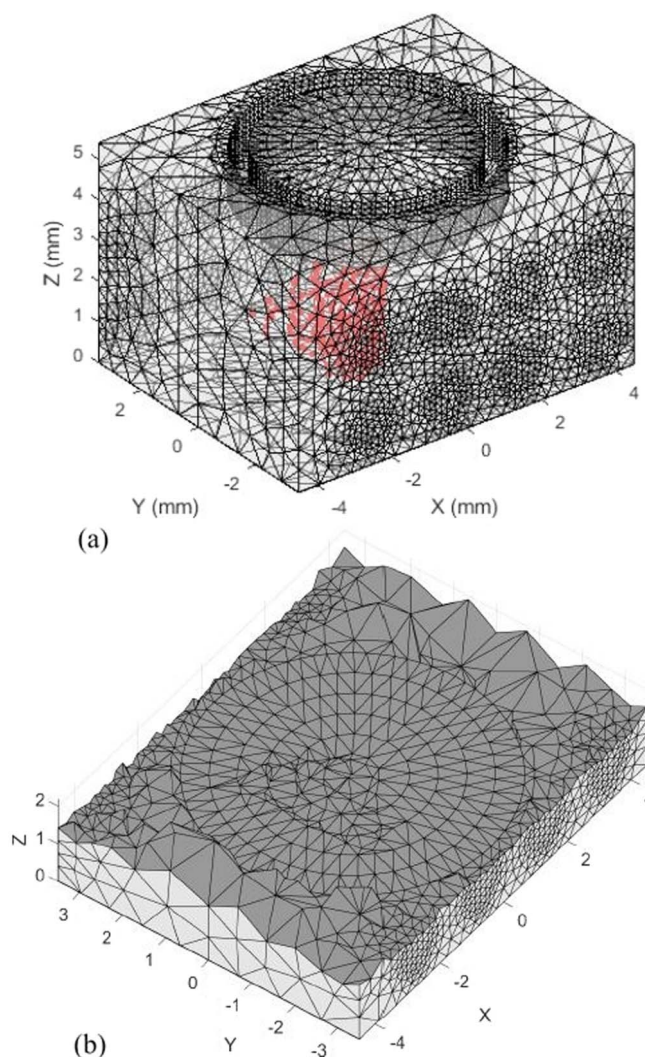


Figure 4. (a) An example of an FE mesh with additional nodes and elements placed in the tissue segment. Nodes in the tissue segment are marked in red. The cylindrical rotational part of the mesh has an outer radius of 3.2 mm. (b) Tetrahedral elements of an example mesh plotted up to a height of 1.2 mm from the chamber bottom. The mesh has been refined inside the tissue segment at the center of the mesh.

conventional reconstruction method is only used in the first experimental study (1) as a reference for the multimodal OPT-mfEIT reconstruction, and (2) to investigate the effect of the number of rotation angles on the 3D R-mfEIT reconstruction. Finally, we describe the multimodal OPT-mfEIT reconstruction, where the structural information provided by OPT is included in R-mfEIT.

Both the conventional and the multimodal reconstructions are in principle absolute image reconstructions. This means that the data, from which the reconstructions are computed, are measured at a single time instant instead of using the difference of two data sets measured at different times or using different frequencies. Additionally, our reconstruction methods include an approximative correction for errors in the modelling of the EIT measurements, which is explained below.

The FE model and reconstruction algorithm were written for Matlab, with modifications to account for rotational data acquisition (Koskela *et al* 2018). For mesh creation, the open-source software Netgen v.4.9.11 was used. R-mfEIT and OPT-mfEIT 3D visualizations were done in Avizo.

2.6.1. Modeling of Rotational EIT Measurements

EIT measurements are modeled by the CEM, which consists of a partial differential equation (3) and three boundary conditions (4)–(6):

$$\nabla \cdot (\sigma \nabla u) = 0, \quad \vec{r} \in \Omega, \quad (3)$$

$$\sigma \frac{\partial u}{\partial \vec{n}} = 0, \quad \vec{r} \in \partial\Omega \setminus \bigcup_{l=1}^L e_l, \quad (4)$$

$$\int_{\{e_l\}} \sigma \frac{\partial u}{\partial \vec{n}} dS = I_l, \quad l = 1, \dots, L, \quad (5)$$

$$u + z_l \frac{\partial u}{\partial \vec{n}} = U_l, \quad \vec{r} \in e_l, \quad l = 1, \dots, L, \quad (6)$$

where σ is the electric conductivity, u is the electric potential inside the target Ω with boundary $\partial\Omega$, \vec{n} is the outward unit normal of the boundary, I_l is the current through electrode e_l , z_l is the contact impedance between electrode e_l and the target, U_l is the potential on electrode e_l , and L is the number of electrodes. EIT measurements are modeled by approximating the CEM with the finite element method (FEM) for given values of σ , z , and given current excitation (Vauhkonen *et al* 1999). In this study, tetrahedral elements are used, and both σ and u are represented by linear basis functions. In addition to (3)–(6), the reference level of electric potential is set, and charge conservation is fulfilled by requiring that

$$\sum_{l=1}^L U_l = 0, \quad (7)$$

$$\sum_{l=1}^L I_l = 0. \quad (8)$$

Approximating the CEM with FEM leads to a matrix equation $A\theta = I$, where A is the system matrix, θ is a vector containing nodal values of u and electrode potentials U , and vector I depends on the current excitation.

In rotational EIT, the overriding idea is to improve EIT measurements' information content by rotating the specimen and carrying out the current excitations and potential measurements sequentially for various rotation angles. This approach significantly improves the EIT reconstructions compared to stationary limited angle EIT. In technical terms, the temporal changes of the conductivity distribution due to rotation are modeled by constructing mappings that deform the electrical conductivity of the initial state to each of the rotational positions and incorporating these mappings into the forward solver of EIT. Lehti-Polojärvi *et al* (2018)

We adopted a previously presented approach to constructing the rotation mappings (Koskela *et al* 2018) but extended it to 3D. In this so-called click method, a rotationally invariant inner boundary in the mesh limits the rotational domain. In the FE mesh, a rotating cylindrical body with a radius of 3.2 mm was modeled in the middle of the rectangular imaging chamber, as shown in figure 4. This radius was selected to be wider than the rotating tube in the experimental setup.

Nodes were placed on the modeled cylinder boundary with an angular spacing of 4.5° , corresponding to the measurements' angular spacing. Rotational measurements were modeled by rotating the cylinder 4.5° in the direction of rotation, thus rotating the conductivity distribution inside the cylinder without deforming the mesh. Performing the rotation in this way only requires re-indexing of the element connectivity table to connect elements inside the rotating cylinder to elements outside it. This index mapping is pre-computed for each rotation angle when the mesh is created. This click method was shown to be faster and resulted in more accurate reconstructions (Koskela *et al* 2018) than simpler approaches based on multiplying the nodal conductivity vector σ by a matrix that approximately computes the rotated conductivity distribution (Lehti-Polojärvi *et al* 2018).

Computing EIT reconstructions iteratively requires computing the Jacobian matrix, that is, derivatives of the electrode potentials with respect to nodal values of σ (Vilhunen *et al* 2002). In rotational EIT image reconstruction, the Jacobian is needed for each rotational position. This computation can be sped up by pre-computing and storing the derivatives $dA/d\sigma$, which appear in the Jacobian formula, for each rotational position when the mesh is created.

2.6.2. Conventional R-mfEIT reconstruction

The inverse problem of EIT is to reconstruct the electrical conductivity σ of the target based on the injected current and measured voltage data. Solving the inverse problem requires inverting the forward model of EIT described above. However, in conventional (R-mf)EIT, where structural constraints are not available, the inverse problem is mathematically ill-posed and its solution requires regularization or use of prior information about the conductivity. In this study, the inverse problem is formulated in the Bayesian framework. EIT measurements are modeled as $V = U(\sigma, z) + e$, where $U(\sigma, z)$ is a FE approximation of the CEM in (3)–(8), and e is a noise vector assumed to be additive. In the Bayesian approach, the electric conductivity σ and measurement noise e are modeled as random variables (Kaipio and Somersalo 2006). The noise vector e is assumed to be Gaussian with zero mean. The covariance Γ_e (2) is estimated based on repeated measurements. Contact impedances are fixed to $z = 1 \Omega$ for each electrode.

In the Bayesian framework, prior information about the unknown conductivity distribution σ is encoded into the prior probability density, which in this study is a multivariate Gaussian smoothness prior characterized by the mean σ^* and covariance matrix Γ_σ . The mean is chosen as the best homogeneous fit to reference data at a given frequency, namely

$$\sigma_*^f = \arg \min_{\sigma} \|L_e^f (V_{ref}^f - U(\sigma, z))\|^2, \quad (9)$$

where L_e^f is the Cholesky factor of the noise precision matrix $(\Gamma_e^f)^{-1}$, that is, $(L_e^f)^T L_e^f = (\Gamma_e^f)^{-1}$. The prior covariance Γ_{σ} used in this work has the form

$$\Gamma(i, j) = a \exp\left(-\frac{\|\vec{r}_i - \vec{r}_j\|^2}{2b^2}\right), \quad (10)$$

where \vec{r}_i is the position vector of the node i , $a = \left(\frac{\sigma_*}{3}\right)^2$, $b = \frac{c}{\sqrt{2 \log 100}}$ and $c = 1$ mm is called the correlation length, which controls the degree of spatial smoothness. Correlation length was chosen based on the approximate expected sizes of the inclusion(s). Details of the smoothness prior, including the interpretation and the choice of parameters, have been previously presented, where a similar prior model was used (Lipponen *et al* 2013).

Using the best-fit homogeneous conductivity σ_* , we also computed a model discrepancy term $\varepsilon^f = U(\sigma_*, z) - V_{ref}^f$, which is used for approximative model error correction in the image reconstruction (Hallaji *et al* 2014). In the present study, such modeling errors may result from the saline level's uncertainty in the imaging chamber, the saline surface's curvature, and possible uncertainty in the excitation current values.

With the above choices for the noise model and prior, the EIT reconstruction for each frequency was obtained as

$$\widehat{\sigma}^f = \arg \min_{\sigma} \|L_e^f (V^f - U(\sigma, z) + \varepsilon^f)\|^2 + \|L_{\sigma}(\sigma - \sigma_*)\|^2, \quad (11)$$

where L_{σ} is the Cholesky factor of the inverse prior covariance Γ_{σ}^{-1} .

For R-mfEIT image reconstruction, we applied an iterative Gauss–Newton method (Heikkinen *et al* 2002). The Gauss–Newton iteration has the form

$$\sigma_{k+1}^f = \sigma_k^f + d(J^T (\Gamma_e^f)^{-1} J + L_{\sigma}^T L_{\sigma})^{-1} (J^T (\Gamma_e^f)^{-1} (V^f - U(\sigma_k, z) + \varepsilon^f) - \Gamma_{\sigma}^{-1}(\sigma_k - \sigma_*)), \quad (12)$$

where the step length d was chosen by a line search method at each iteration (Karhunen *et al* 2010). As an initial point of iteration, σ_0^f , we use the best-fit homogeneous conductivity σ_*^f .

2.6.3. OPT-mfEIT reconstruction

In the OPT-informed mfEIT, the model for the electrical measurements is the same as in the conventional single-modality case: the dependence between electric conductivity and electrode potentials is described by CEM (3)–(8), and the model is approximated numerically using FEM. Also, the rotational setup is modeled as described above. The difference between the conventional R-mfEIT and the proposed OPT-mfEIT is that in the latter reconstruction, the segmentation obtained from OPT is used as a geometrical constraint for the electrical conductivity distribution σ . More specifically, the conductivity inside each segment is assumed to be homogeneous at any given frequency.

The benefit of utilizing the assumption of segmentally constant conductivity is that it dramatically decreases the number of unknown parameters in EIT imaging. In this study's experiments, the number of conductivity parameters at each frequency in OPT-mfEIT varies between 2 and 3. In contrast, in the conventional R-mfEIT, thousands of unknown conductivity parameters were reconstructed based on the electrode potential data at each frequency. This low order parameterization decreases the computational complexity and computation time from the conventional R-mfEIT case and—above all—stabilizes the originally ill-posed inverse problem of EIT and potentially leads to more reliable estimates of the tissue's conductivity spectrum. For this reason, a prior function is not required to compute the reconstructions, unlike in the conventional mfEIT reconstruction.

In the experiments performed in this study, the OPT reconstructions provided the following main segments: one or two inclusions, the FEP tube, and the background. The inclusion(s) and the background were considered as subvolumes, each having constant unknown conductivity at a given frequency. The FEP tube was modeled as a perfect insulator. Consequently, the tube segment's surface was modeled as a boundary of the computational domain in R-mfEIT; on this boundary, the zero-flux boundary condition (4) was assigned equivalently to all other electrode-free boundaries of the computational domain.

The segment conductivities at each frequency were computed by solving a minimization problem of the form

$$\widehat{\sigma}_s^f = \arg \min_{\sigma_s} \|L_e^f (V^f - U(F(\sigma_s), z) + \varepsilon^f)\|^2, \quad (13)$$

where $\sigma_s = [\sigma_1, \dots, \sigma_{N_s}]^T$, N_s is the number of segments, and F maps the conductivity values σ_s to the nodal conductivity values in the mesh.

The Gauss–Newton method was also used for the segmentation-based OPT-mfEIT reconstruction with slight modifications. In this case, the iteration has the form

$$\sigma_{k+1}^f = \sigma_k^f + d(J_s^T (\Gamma_e^f)^{-1} J_s)^{-1} J_s^T (\Gamma_e^f)^{-1} (V^f - U(\sigma, z) + \varepsilon^f), \quad (14)$$

where σ now denotes the conductivities of the segments, that is, $\sigma = [\sigma_1, \dots, \sigma_{N_s}]^T$, where N_s is the number of segments. Moreover, J_s is the Jacobian matrix of the measurements with respect to the segment conductivities, defined as $J_s = JP$, where P is a $N_n \times N_s$ matrix, which maps the segment conductivity values to the N_n nodes in the mesh.

2.6.4. Meshing

The imaging volume, excluding the tube segment, was first meshed with Netgen. The segmentation was then used to refine the mesh by increasing the mesh density at the tissue's location, as shown in figure 4. Since the FEP tube is a good electrical insulator, the boundary condition of zero normal current density (4) was imposed on the tube boundary, and the tube volume was not meshed. Each mesh used in this study had approximately 11 000 nodes. The center-of-rotation correction performed in the OPT reconstructions was not considered in the R-mfEIT reconstructions. The offset values were typically close to zero and a maximum of 44 pixels, which corresponded to 143 μm . These offsets were not considered a significant source of error in the R-mfEIT reconstructions.

2.7. Materials and specimens

We performed four experiments with different specimen types to demonstrate the feasibility of the proposed technique. The imaging chamber was filled with phosphate buffered saline (PBS, Sigma-Aldrich PBS tablet in purified Milli-Q water, concentration 0.01 M phosphate buffer, 0.0027 M KCl and 0.137 M NaCl). All specimens were prepared into 5 mm inner diameter FEP tubes. Agarose gel 1.5% (w/w) (low gelling powder, Sigma Life Science) was prepared in PBS. Phantom and tissue inclusions were manually cut to approximately 1 mm \times 1 mm \times 1.5 mm sized pieces. One or two inclusions were placed at the bottom of the tube, and 200 μl of agarose was pipetted on top. All specimens were left to gelate and stabilize at room temperature for at least 15 min before imaging. All measurements were acquired at room temperature.

In Experiment 1, a tetrahedral piece of fresh potato was embedded in agarose. The potato phantom was chosen due to its well-known electrical properties.

Experiment 2 was performed with fresh human subcutaneous adipose tissue (female donor with normal Body Mass Index) with written informed consent in accordance with the Regional Ethics Committee of the Expert Responsibility area of Tampere University Hospital, Tampere, Finland (ethical approval R15161). The aim was to investigate the OPT-mfEIT capability to differentiate viable and thermally killed tissues. The first specimen contained a viable piece of adipose tissue that was imaged within 24 h of cutting. To induce necrotic cell death, another specimen was prepared by placing a tissue piece on aluminum foil and kept on top of dry ice (approximately -79°C) for 55 min before embedding it in agarose.

To investigate the ability of OPT-mfEIT to distinguish between intact and broken cell membranes, we used fresh and chemically treated porcine liver tissue in Experiment 3. Porcine liver tissue was purchased from a local abattoir, and all measurements were performed within 14 h of extraction. Triton X-100 is commonly used to lyse cells in biological research. We prepared 2% (v/v) solution by diluting Triton X-100 (Sigma-Aldrich, Inc. USA) with PBS. Before embedding the inclusions in agarose, the treated tissue pieces were incubated in the solution for 1 h and then washed with PBS for 15 min to rinse the Triton X-100 residues from the tissue. We studied four specimens: liver 1 (one piece of fresh liver), liver 2 (one piece of treated liver), liver 3 and 4 (one piece of fresh and one piece of treated liver in each specimen).

In Experiment 4, iPSCs embedded in biomaterial spheroids were imaged to investigate the ability of OPT-mfEIT to detect tissue engineered inclusions. The iPSCs (cell line UTA.10211.EURCCs, ethical approval R12123) were cultured on Geltrex-coated plates in mTesR1 medium (Stemcell) at 37°C in 5% CO_2 . The cells were collected from the cell culture plates by incubating them with Versene at 37°C for 4 min and collecting them into mTesR1 medium. Cell suspension was centrifuged with $150 \times g$ for 5 min, washed with 10% sucrose twice, and finally resuspended in 10% sucrose. Then, the cell suspension was mixed with biomaterial (Puramatrix, Corning, USA) and Collagen I (Gibco) solution. iPSC spheroids were created by pipetting 5 μl droplets of the cell-biomaterial mix into cell culture medium on a 48 well plate, and thereby creating spheroids with a diameter of approximately 1 mm. The spheroids were then immediately embedded in agarose and imaged within 7 h. To clarify the effect of the cells on specimen conductivity, we also imaged two biomaterial spheroids without cells. We studied four specimens: cells 1 (one biomaterial spheroid with cells), cells 2 (two biomaterial spheroids with cells), biomaterial 1 and 2 (one blank biomaterial spheroid).

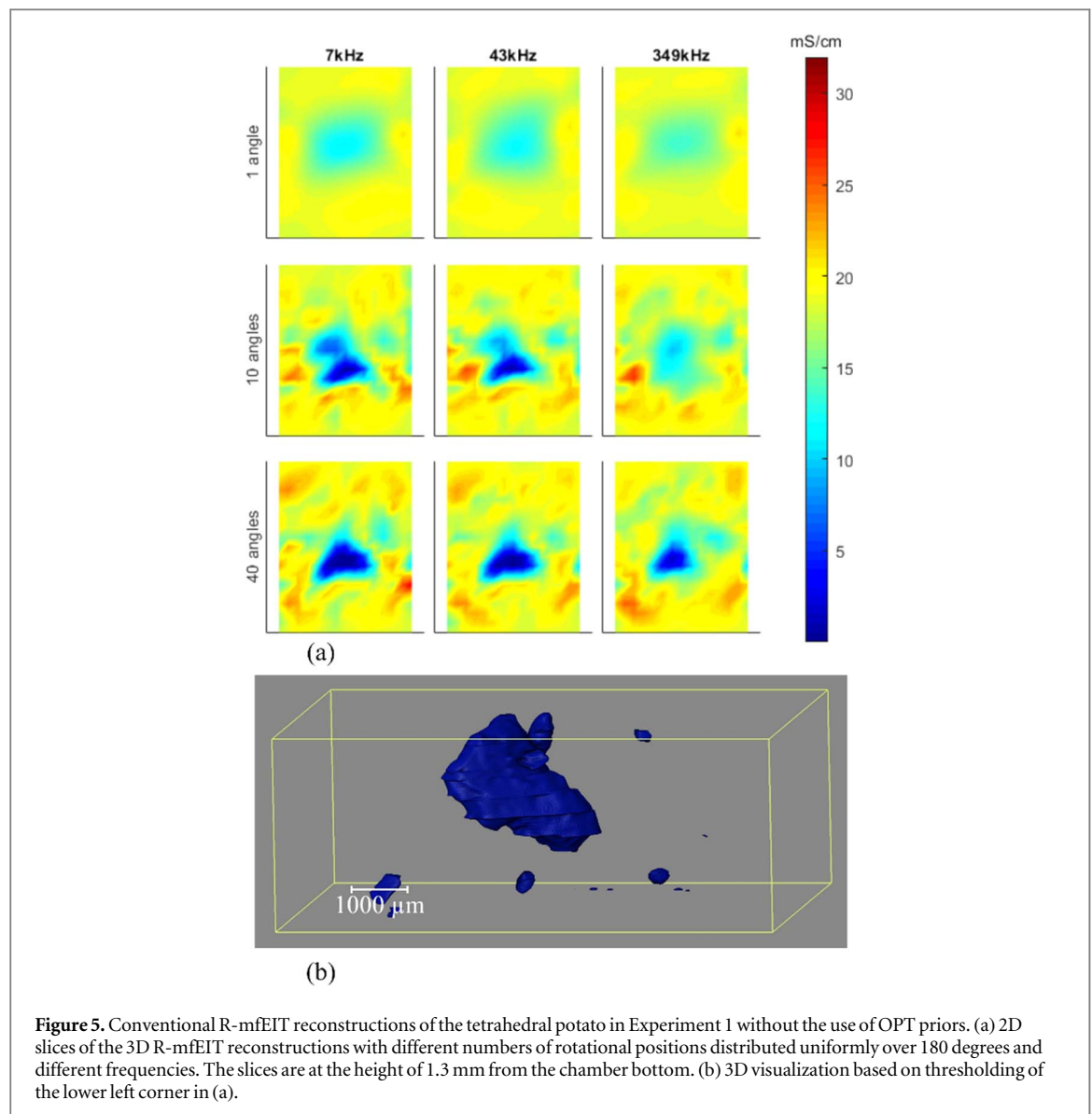


Figure 5. Conventional R-mfEIT reconstructions of the tetrahedral potato in Experiment 1 without the use of OPT priors. (a) 2D slices of the 3D R-mfEIT reconstructions with different numbers of rotational positions distributed uniformly over 180 degrees and different frequencies. The slices are at the height of 1.3 mm from the chamber bottom. (b) 3D visualization based on thresholding of the lower left corner in (a).

3. Results

The results of Experiment 1 are presented in figures 5 and 6. These figures illustrate the reconstruction of conventional R-mfEIT (figure 5) and the OPT-mfEIT (figure 6), according to the steps described in the flowchart in figure 1. For Experiments 2–4, only the main results are shown in the figures: the tissue conductivity spectrum and one 3D visualization at 7 kHz, as in figures 6(c) and (d).

The 2D slices of the conventional 3D R-mfEIT reconstructions in figure 5(a) clearly show that the potato is less conductive than the background. The estimated conductivity of the potato increases with increasing AC frequency from 7 to 349 kHz. The background conductivity is not, however, affected by the frequency change.

Increasing the number of measurement angles enhances image quality, as the shape of the inclusion is detected more accurately with 40 angles than with 10 angles in 180° rotation in figure 5(a). One angle—one measurement set with the 16-electrode setup—is not enough to provide reasonable images in our limited angle R-mfEIT setup. We therefore chose to use 40 angles to compute all further results.

Figure 5(b) shows a 3D illustration of the conventional R-mfEIT at 7 kHz (thresholding 8.5 mS cm^{-1}). Although some imaging artifacts are present, the R-mfEIT captures the shape of the potato relatively well. This result implies that R-mfEIT can provide valuable information on the spatially distributed conductivity within the imaging domain. This result is an encouraging observation, as in the multimodal OPT-mfEIT, the reconstruction quality is further enhanced.

The OPT-mfEIT results for the potato are shown in figure 6. The OPT reconstruction (figure 6(a)) was used to segment electrically relevant regions (figure 6(b)), where the potato specimen and the FEP tube are depicted with different colors, whereas the background is transparent. The OPT-mfEIT reconstruction at 7 kHz is

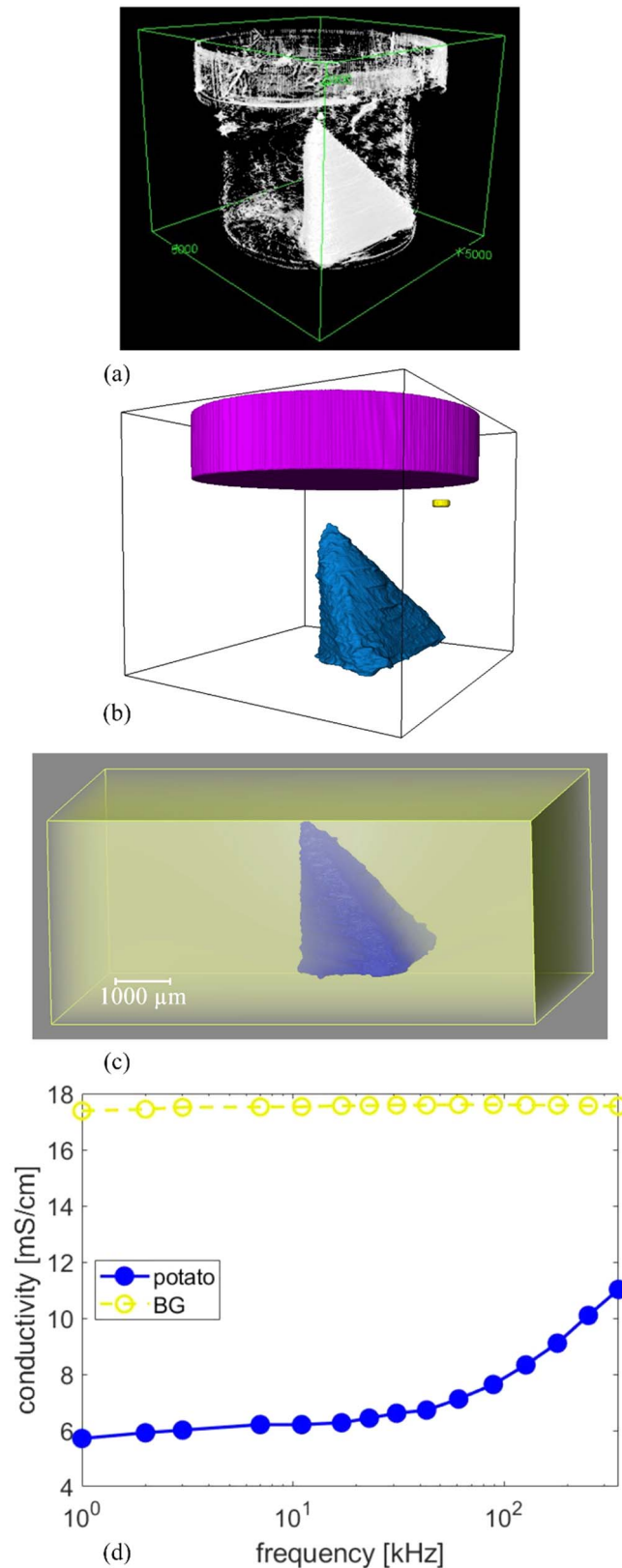
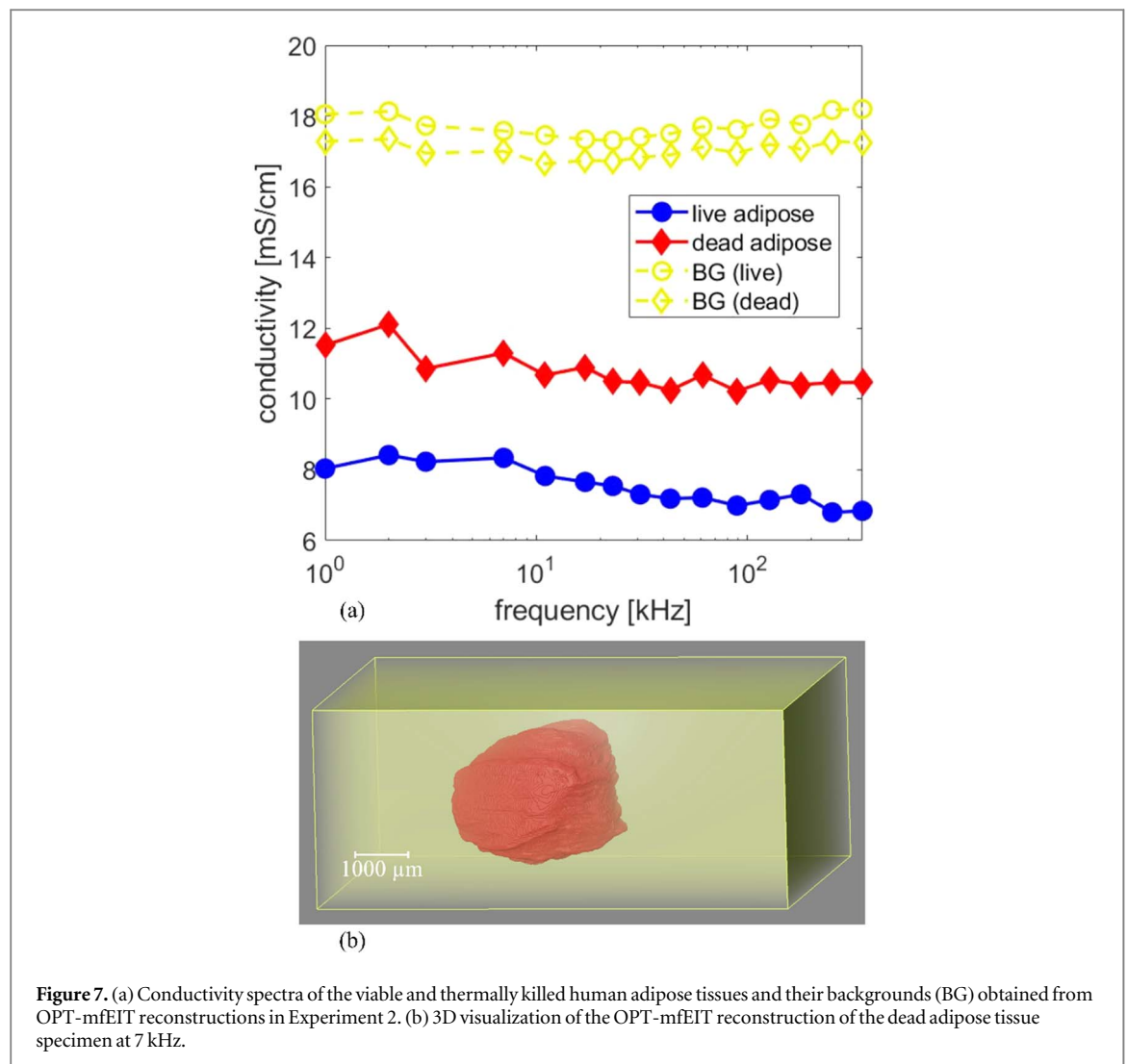


Figure 6. Retrieval of conductivity spectrum of a tetrahedral piece of potato using OPT-mfEIT reconstructions in Experiment 1. (a) OPT reconstruction showing the potato, agarose, and FEP tube in transparent saline. (b) Potatoes (blue), tube (magenta), and a marker (yellow) segmented from (a). (c) Example of one OPT-mfEIT reconstruction at 7 kHz illustrating potato (blue) and background (yellow). (d) Estimated conductivity spectra of the potato segment (blue) and background segment (BG, yellow) in the range of 1–349 kHz. Each conductivity value is obtained from a reconstructed 3D OPT-mfEIT image as shown in (c).



visualized in figure 6(c), and the conductivity spectra of the potato and the background in figure 6(d). As in conventional R-mfEIT, the background is more conductive than the potato inclusion. Also, the potato's conductivity increases as the applied frequency increases, whereas the background remains nearly constant.

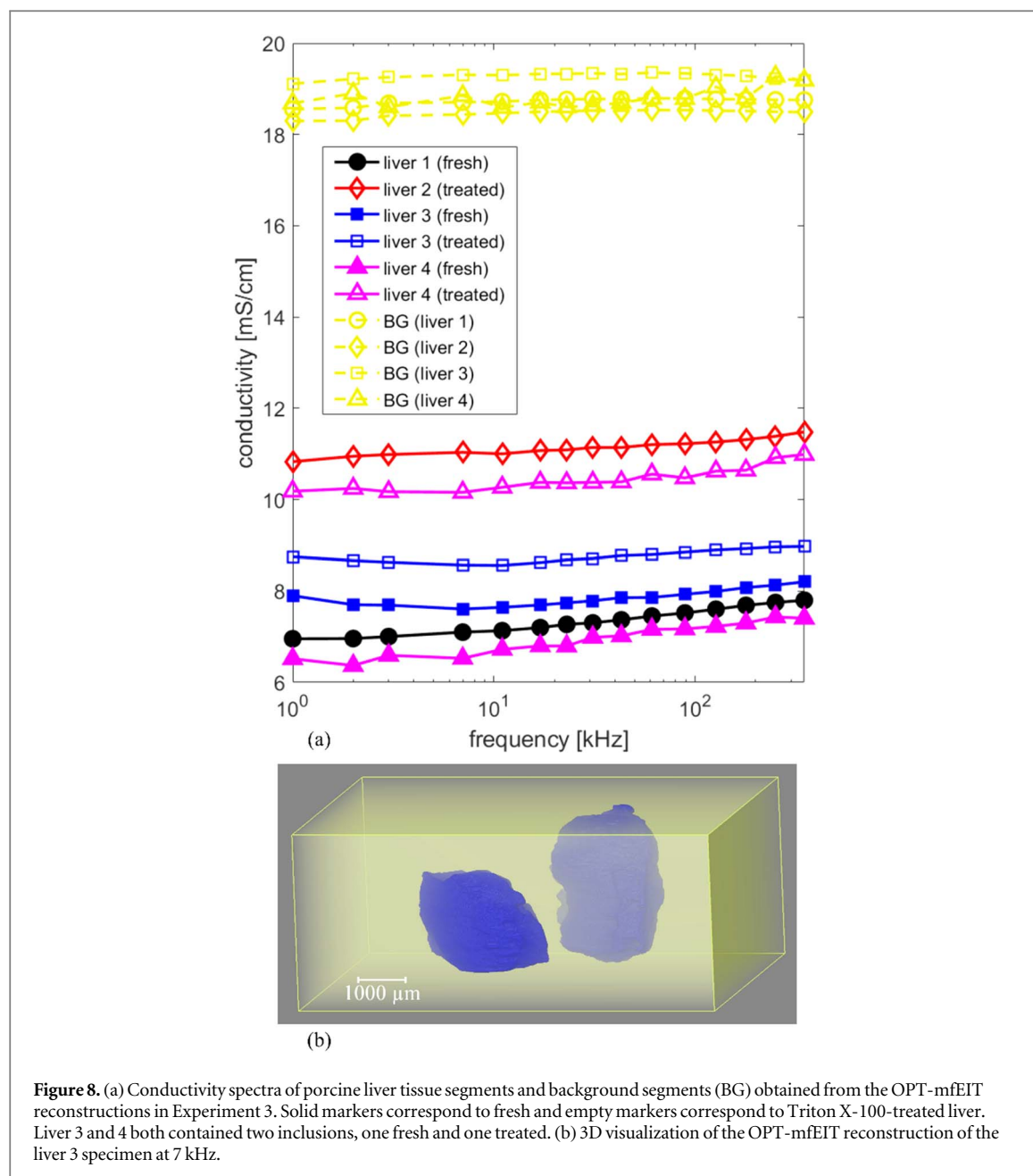
The OPT-mfEIT results of Experiment 2 on human adipose tissue are shown in figure 7. The dead tissue is more resistive than the background, and the viable tissue is more resistive than the dead tissue. The background conductivities are approximately the same as in Experiment 1.

The porcine liver tissues conductivity spectra of Experiment 3 are shown in figure 8. Regardless of the specimen containing one or two inclusions, the estimated conductivities of all Triton X-100-treated inclusions are higher than the conductivities of the fresh liver inclusions. All background conductivity values are close to those in Experiments 1 and 2.

The estimated conductivity spectra for iPSCs and the biomaterial spheroids in Experiment 4 are shown in figure 9. The blank biomaterial appears more conductive than the background and the iPSC-containing biomaterial spheroids. The background spectra are close to those in Experiments 1–3.

4. Discussion and conclusions

The results of the experimental studies clearly show the power of multimodal tomography and the use of OPT as prior for R-mfEIT. The conventional, single-modality R-mfEIT reconstructions in Experiment 1 are of typical absolute EIT image quality, representing the shape, location, and conductivity of the inclusion relatively well (figure 5). The spatial resolution of OPT-mfEIT, however, is superior to the R-mfEIT reconstruction seen in figures 6–9. Furthermore, although the potato conductivity provided by the conventional R-mfEIT was in the same range as that provided by OPT-mfEIT (compare figures 5 and 6), the smoothness and image artifacts in conventional R-mfEIT make the quantitative analysis of conductivity spectra difficult from these EIT images. In



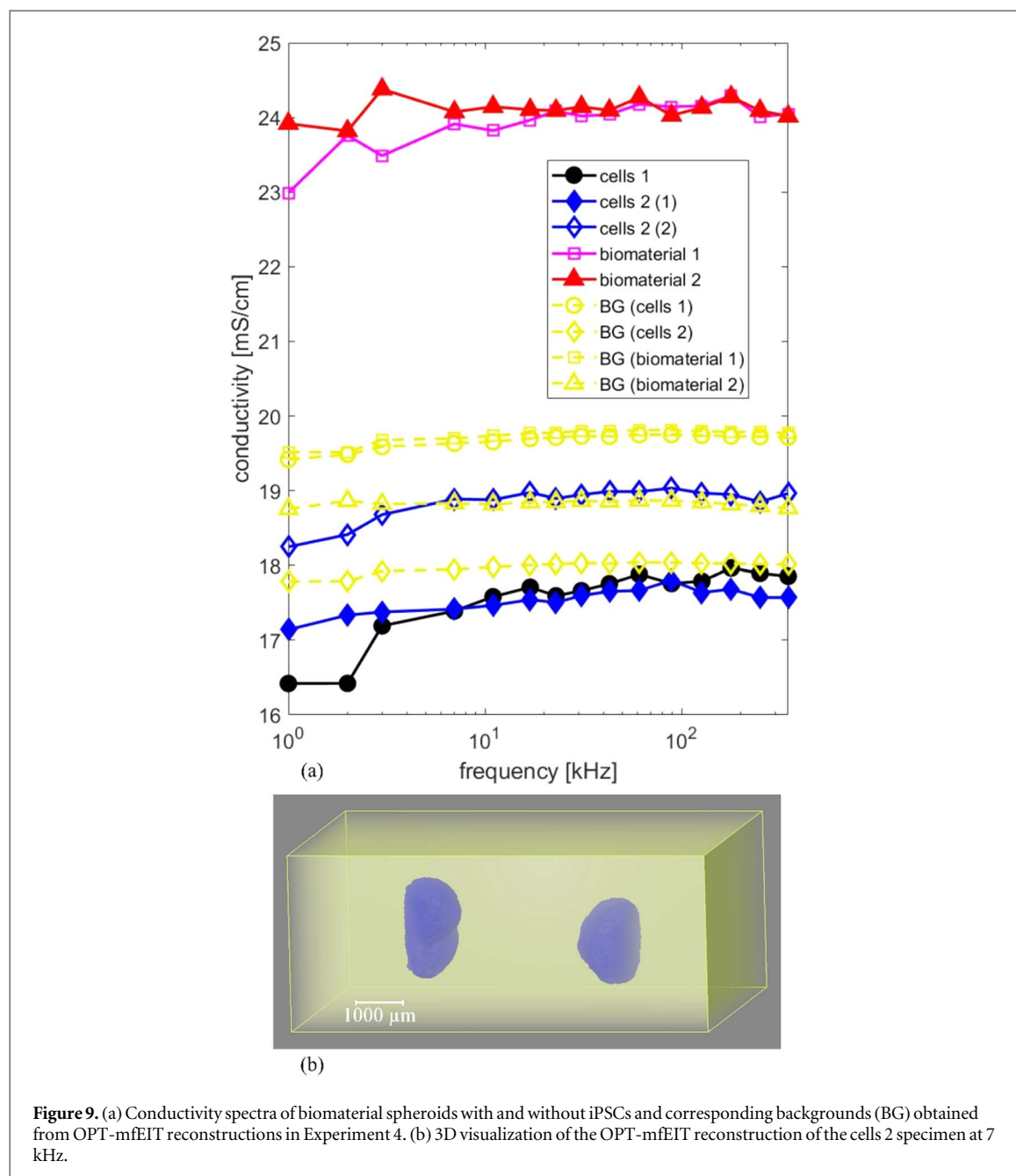
OPT-mfEIT, the conductivity spectra can be directly extracted from the reconstructed frequency-dependent (but inclusion-wise constant) conductivities.

Increasing the number of rotational positions in figure 5 (a) enhanced the image quality. This effect is due to the rotational measurement protocol increasing the number of independent measurements compared to stationary EIT. Similar results have been shown in 2D (Lehti-Polojärvi *et al* 2018).

The background segments' conductivity was assumed to be homogenous in all OPT-mfEIT reconstructions. This segment consisted of the PBS solution and the agarose gel in all experiments. Since agarose was prepared in PBS, the assumption of background homogeneity was justified. The reconstructed background conductivities were close to 18 mS cm^{-1} in all experiments indicating stability of OPT-mfEIT. This value is somewhat higher than our directly measured values of 12 mS cm^{-1} for PBS and 13 mS cm^{-1} for agarose (conductivity meter, Hanna Instruments, HI-8733) at room temperature.

The potato results in Experiment 1 show a clear increase in conductivity at high frequencies (from 6 mS cm^{-1} to 11 mS cm^{-1}), suggesting that the potato cell walls were intact, acting resistively at low frequencies and passing more current at higher frequencies. These results are in accordance with a previous study that show an increase of potato conductivity from 0.25 to 4.5 mS cm^{-1} at the same frequency range (Ahn *et al* 2010).

The adipose tissues in Experiment 2 (figure 7) showed relatively flat conductivity spectra at the used frequency range as was expected (Gabriel *et al* 1996). Killing the adipose tissue by freezing is expected to cause necrotic cell death that includes the breakdown of cell membranes, allowing the current to flow through the well



conducting cytoplasm. This effect caused the conductivity to increase after freezing, which is in accordance with a previous study on rat liver (Davalos and Rubinsky 2004).

The porcine liver inclusions in Experiment 3 (figure 8) show a modest but consistent increase of conductivity along with increasing frequency as was expected (Gabriel *et al* 1996). After treatment by Triton X-100 solution, liver tissues indicate an increase in conductivity due to the breakdown of cell membranes, allowing current to pass the well conducting cytoplasm. These results are in line with previous studies on, for example, the Triton X-100 treatment of breast cancer spheroids (Wu *et al* 2018).

The iPSCs and biomaterial spheroids were challenging specimens, as they only covered approximately 0.5% of the whole measured volume. Also, inside the spheroids, there was biomaterial between the iPSCs with no developed cell–cell junctions. However, our results show that we can detect the presence of iPSCs in the spheroids, as they decreased the conductivity compared to the blank biomaterial in Experiment 4 (figure 9). This was expected since the iPSCs can be assumed viable and thus resistive at the used frequency range. Also, iPSC spheroids showed flat conductivity spectra that were expected at the used frequency range and tetrapolar measurement scheme (Canali *et al* 2015).

The mfEIT device used in this study did not provide the accurate excitation current values, and thus a nominal value of 1 mA was used in the forward model for each excitation. This approximation may be one reason for the estimated conductivities of potato, tissues, and background to be higher than reference values in

the literature (Gabriel *et al* 1996, Ahn *et al* 2010) and direct measurements. In general, EIT measurements and obtained conductivity values are dependent on the measurement system and the temperature and condition of the specimen. Thus, direct comparison of the conductivity values between different studies is difficult. Moreover, it is more meaningful to compare the changes occurring in the same specimen type and measurement conditions.

Overall, the conductivity values and the frequency responses obtained were in good agreement with previous knowledge considering the general difficulty of measuring the conductivity of very small soft objects. Typically, tissue conductivity would have to be estimated based on impedances measured within a chamber with known dimensions. In future studies, one interesting possibility is to compare the OPT-mfEIT conductivity spectra with impedance spectra obtained, for example, by bioimpedance-based needle providing a defined and known measurement volume (Halonen *et al* 2019).

The volume of the inclusions in our experiments only covered from 0.5% to 5.6% of the total measured volume, being highest for adipose tissues and smallest for the iPSC spheroids. Thus, OPT-mfEIT proved to be an effective technique even for low volume fraction specimens.

The data acquisition time induces a possible error source in our measurements because some of the saline typically evaporated during imaging. Also, due to the small size of the imaging chamber and the surface tension of the PBS, the saline surface had a significant curvature (seen in the OPT raw data videos in supplementary materials). These factors can cause geometric modeling errors in our R-mfEIT model, affecting the reconstructions' accuracy. An approximative method was used to correct for modeling errors using a reference R-mfEIT measurement. In future, the imaging system could be improved to reduce these uncertainties, or the reconstruction methods could be modified to take these modeling errors into account more accurately.

Our 3D reconstruction algorithms were relatively time-efficient since the conventional R-mfEIT took approximately 37 min and the OPT-mfEIT approximately 21 min for each frequency with 40 angles. Computations were performed on a desktop PC with i5-7500 3.4 GHz CPU and 16 GB RAM.

In the future, the image processing could be automatized to enable faster throughput. This would be feasible with, for example, cell spheroids that were straightforward to segment with simple thresholding operations. We also note that concave or hollow opaque samples are not optimal for OPT because some parts might be undetected in the OPT reconstruction.

As shown in this study, OPT-mfEIT imaging can be used to extract qualitative information about 3D cell and tissue cultures, such as the breakdown of cell membranes and cell death or the presence of stem cells in biomaterial scaffold. To achieve these results, we have built a novel imaging system and enhanced the rotational EIT image reconstruction via segmented OPT data, FEM rotational meshing and modeling, and a nonlinear Bayesian image reconstruction algorithm. Our tool provides a new avenue to study live cells in *in vitro* culturing for various specimen types and applications, ranging from following cell culture growth to cell–cell junctional development or disintegration. This tool will be of interest, for example, in drug development and disease modeling.

Acknowledgments

This work was supported in part by the Finnish Centre of Excellence in Inverse Modelling and Imaging (award 303801) and the Finnish Cultural Foundation (Pohjois-Savon Rahasto), and in part by the Centre of Excellence in Body-on-Chip (awards 326580, 336784) and Emil Aaltonen Foundation. The authors would like to thank the impedance group (Thomas Johann Seebeck Department of Electronics at Tallinn University of Technology) for collaborating on the mfEIT device and electrode fabrication. The corresponding author, M L-P would like to thank MSc Markus Hannula for guidance in image segmentation. We are thankful to MSc Olli Koskela for providing insights into the writing and MA Peter Heath for reviewing the spelling and grammar of this work.

Conflicts of interest

The authors report no conflicts of interest.

ORCID iDs

M Lehti-Polojärvi  <https://orcid.org/0000-0001-9826-5741>

M J Räsänen  <https://orcid.org/0000-0002-4608-7901>

L E Viiri  <https://orcid.org/0000-0003-2279-0392>

H Vuorenpää  <https://orcid.org/0000-0002-6351-3044>

S Miettinen  <https://orcid.org/0000-0002-0647-9556>

A Seppänen  <https://orcid.org/0000-0002-4042-2254>

J Hyttinen  <https://orcid.org/0000-0003-1850-3055>

References

- Ahn S, Jun S C, Seo J K, Lee J, Woo E J and Holder D 2010 Frequency-difference electrical impedance tomography: phantom imaging experiments *J. Phys.: Conf. Ser.* **224** 012152
- Belay B, Koivisto J T, Parraga J, Koskela O, Montonen T, Kellomäki M, Figueiras E and Hyttinen J 2021 Optical projection tomography as a quantitative tool for analysis of cell morphology and density in 3D hydrogels *Sci. Rep.* **11** 6538
- Borsic A, Halter R, Wan Y, Hartov A and Paulsen K D 2010 Electrical impedance tomography reconstruction for three-dimensional imaging of the prostate *Physiol. Meas.* **31** S1–16
- Canali C, Heiskanen A, Muhammad H B, Høyum P, Pettersen F J, Hemmingsen M, Wolff A, Dufva M, Martinsen Ø G and Emnéus J 2015 Bioimpedance monitoring of 3D cell culturing—complementary electrode configurations for enhanced spatial sensitivity *Biosens. Bioelectron.* **63** 72–9
- Davalos R and Rubinsky B 2004 Electrical impedance tomography of cell viability in tissue with application to cryosurgery *J. Biomech. Eng.* **126** 305–9
- Fang Y and Eglen R M 2017 Three-dimensional cell cultures in drug discovery and development *SLAS Discovery* **22** 456–72
- Figueiras E et al 2014 Optical projection tomography as a tool for 3D imaging of hydrogels *Biomed. Opt. Express* **5** 3443–9
- Gabriel S, Lau R W and Gabriel C 1996 The dielectric properties of biological tissues: II. Measurements in the frequency range 10 Hz–20 GHz *Phys. Med. Biol.* **41** 2251–69
- Geselowitz D B 1971 An application of electrocardiographic lead theory to impedance plethysmography *IEEE Trans. Bio-Med. Eng.* **18** 38–41
- Gomes M E, Rodrigues M T, Domingues R M A and Reis R L 2017 Tissue engineering and regenerative medicine: new trends and directions—a year in review *Tissue Eng. B* **23** 211–24
- Hallaji M, Seppänen A and Pour-Ghaz M 2014 Electrical impedance tomography-based sensing skin for quantitative imaging of damage in concrete *Smart Mater. Struct.* **23** 085001
- Hälonen S, Kari J, Ahonen P, Kronström K and Hyttinen J 2019 Real-time bioimpedance-based biopsy needle can identify tissue type with high spatial accuracy *Ann. Biomed. Eng.* **47** 836–51
- Heikkinen L, Vilhunen T, West R and Vauhkonen M 2002 Simultaneous reconstruction of electrode contact impedances and internal electrical properties: II. Laboratory experiments *Meas. Sci. Technol.* **13** 1855–61
- Kaipio J, Kolehmainen V, Vauhkonen M and Somersalo E 1999 Inverse problems with structural prior information *Inverse Problems* **15** 713–29
- Kaipio J and Somersalo E 2006 *Statistical and Computational Inverse Problems* (Berlin: Springer Science & Business Media)
- Karhunen K, Seppänen A, Lehtikoinen A, Monteiro P and Kaipio J 2010 Electrical resistance tomography imaging of concrete *Cement Concr. Res.* **40** 137–45
- Klösgen B, Rümennapp C and Gleich B 2011 Bioimpedance spectroscopy *BetaSys, Systems Biology 2* ed B Boof-Bavnbek et al (Berlin: Springer) pp 241–71
- Koskela O, Chowdhury M T K, Montonen T, Belay B, Pursiainen S and Hyttinen J 2021 Optical projection tomography for particle counting and morphology analysis *8th European Medical and Biological Engineering Conf.* vol 80 (Berlin: Springer) pp 944–51 (IFMBE Proc.)
- Koskela O, Lehti-Polojärvi M, Seppänen A, Figueiras E and Hyttinen J 2018 Finite element mapping for efficient image reconstruction in rotational electrical impedance tomography *World Congress on Medical Physics and Biomedical Engineering 68/2* ed L Lhotska et al (Berlin: Springer) pp 901–4 (IFMBE Proceedings)
- Lehti-Polojärvi M, Koskela O and Hyttinen J 2021 Multifrequency electrical impedance tomography in biological applications: a multimodal perspective *Bioimpedance and Spectroscopy* ed P Annus and M Min (Elsevier Inc.: Academic press) pp 157–89
- Lehti-Polojärvi M, Koskela O, Seppänen A, Figueiras E and Hyttinen J 2018 Rotational electrical impedance tomography using electrodes with limited surface coverage provides window for multimodal sensing *Meas. Sci. Technol.* **29** 025401
- Lehti-Polojärvi M, Koskela O, Seppänen A, Rist M, Land R, Annus P, Min M, Figueiras E and Hyttinen J 2019 EIT in hybrid imaging setup for tissue engineering applications *Proc. 20th Int. Conf. on Biomedical Applications of Electrical Impedance Tomography (London)* ed A Boyle et al (London, UK) (<https://doi.org/10.5281/zenodo.2691705>)
- Lipponen A, Seppänen A and Kaipio J P 2013 Electrical impedance tomography imaging with reduced-order model based on proper orthogonal decomposition *J. Electron. Imaging* **22** 023008
- Liu Z, Kang X, Bagnaninchi P and Yang Y 2020 Impedance-optical dual-modal sensor and image reconstruction for cell spheroids imaging *2020 IEEE SENSORS* pp 1–4
- Min M, Lehti-Polojärvi M, Hyttinen J, Rist M, Land R and Annus P 2018 Bioimpedance spectro-tomography system using binary multifrequency excitation *Int. J. Bioelectromagn.* **20** (1) 76–9
- Natterer F 2001 *The mathematics of computerized tomography* (Philadelphia, PA: Society for Industrial and Applied Mathematics)
- Savolainen V, Juuti-Uusitalo K, Onnela N, Vaajasaari H, Narkilahti S, Suuronen R, Skottman H and Hyttinen J 2011 Impedance spectroscopy in monitoring the maturation of stem cell-derived retinal pigment epithelium *Ann. Biomed. Eng.* **39** 3055–69
- Sharpe J, Ahlgren U, Perry P, Hill B, Ross A, Hecksher-Sørensen J, Baldock R and Davidson D 2002 Optical projection tomography as a tool for 3D microscopy and gene expression studies *Science* **296** 541–5
- Soleimani M 2006 Electrical impedance tomography imaging using *a priori* ultrasound data *Biomed. Eng. Online* **5** 1–8
- Tamminen I, Lehto K, Hannula M, Ojansivu M, Johansson L, Kellomäki M, Miettinen S, Aula A, Ihalainen T and Hyttinen J 2020 A tube-source x-ray microtomography approach for quantitative 3D microscopy of optically challenging cell-cultured samples *Commun. Biol.* **3** 1–13
- Vauhkonen P, Vauhkonen M, Savolainen T and Kaipio J 1999 Three-dimensional electrical impedance tomography based on the complete electrode model *IEEE Trans. Biomed. Eng.* **46** 1150–60
- Vilhunen T, Kaipio J, Vauhkonen P, Savolainen T and Vauhkonen M 2002 Simultaneous reconstruction of electrode contact impedances and internal electrical properties: I. Theory *Meas. Sci. Technol.* **13** 1848–54
- Winkler S, Lehti-Polojärvi M and Hyttinen J 2020 Hyperparameter algorithms in electrical impedance tomography for rotational data *Proc. EMBEC 2020* ed T Jarm (Berlin: Springer) pp 631–43
- Wu H, Yang Y, Bagnaninchi P O and Jia J 2018 Electrical impedance tomography for real-time and label-free cellular viability assays of 3D tumour spheroids *Analyst* **143** 4189–98
- Yuan Q 2020 A modular labview program for controlling multimodal microscope imaging platform *MS Thesis* Tampere University <http://urn.fi/URN:NBN:fi:tuni-202004284176>